Shape Reconstruction by Learning Differentiable Surface Representations

Jan Bednařík Shaifali Parashar Erhan Gündoğdu Mathieu Salzmann Pascal Fua
CVLab, EPFL, Switzerland
{firstname.lastname}@epfl.ch

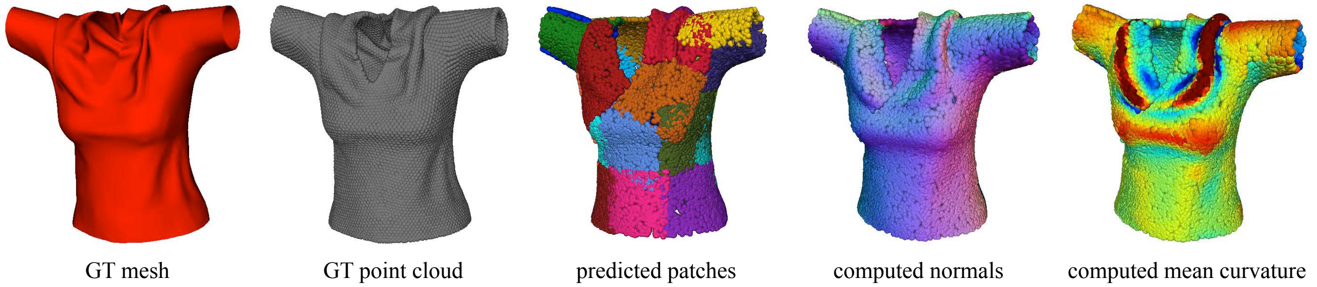

Figure 1. **Our method predicts a multi-patch representation where the patches are guaranteed not to collapse and to minimally overlap.** Thanks to its explicit access to the surface's differential properties, our method computes normals and curvature *analytically* for any predicted point of the modeled surface.

Abstract

Generative models that produce point clouds have emerged as a powerful tool to represent 3D surfaces, and the best current ones rely on learning an ensemble of parametric representations. Unfortunately, they offer no control over the deformations of the surface patches that form the ensemble and thus fail to prevent them from either overlapping or collapsing into single points or lines. As a consequence, computing shape properties such as surface normals and curvatures becomes difficult and unreliable.

In this paper, we show that we can exploit the inherent differentiability of deep networks to leverage differential surface properties during training so as to prevent patch collapse and strongly reduce patch overlap. Furthermore, this lets us reliably compute quantities such as surface normals and curvatures. We will demonstrate on several tasks that this yields more accurate surface reconstructions than the state-of-the-art methods in terms of normals estimation and amount of collapsed and overlapped patches.

1. Introduction

Point clouds are becoming increasingly popular as a compact and expressive way to represent 3D surfaces because they can capture high frequency geometric details without requiring much memory. State-of-the-art methods rely on encoder/decoder architectures to create latent representations from input data and then decode them using one or more learned mappings from a 2D parameter space to the 3D surface. Each one of these mappings can be thought of as transforming a 2D rectangular patch into a set of 3D points lying on the surface to be modeled. FoldingNet [33] and AtlasNet [16] are among the best representatives of this approach, and the move from one single patch to multiple ones has proved effective to achieve higher accuracy.

However, this increase in accuracy comes at a price. Nothing guarantees that each patch will represent a substantial portion of the target surface and some may in fact collapse, meaning that they generate a single point or a line instead of a surface-like cloud. Another potential problem is that the 3D clouds generated by different patches will overlap so that the same parts of the underlying surface are represented by several patches, thus resulting in potential inconsistencies across the patches and ineffectively using the decoder's capacity. While these problems may not occur when the training data contains many diverse categories of objects, such as when using the whole of ShapeNet dataset [10], they become apparent in practical scenarios where one aims to model the shape of a specific surface, such as a piece of clothing, as shown in Fig. 1.

In this paper, we address these two issues by leveraging the observation that first and second derivatives of the de-

This work was supported in part by the Swiss National Science Foundation.

coder output can be used to compute the differential properties of the reconstructed surface, without having to triangulate it. In other words, we can compute *exact* surface properties *analytically*, rather than having to approximate these quantities using the point cloud or a mesh. This enables us to incorporate into our training loss function terms that prevent patch collapse and strongly reduce patch overlap.

In our experiments, we will show that being able to compute differential properties and to exploit them during training (1) fully prevents any type of patch collapse, (2) substantially reduces the amount of patch overlap (3) lets us predict surface normals with higher accuracy than SotA.

Our approach to exploiting differentiability is not tied to a specific architecture and we will show on several tasks that it yields not only state-of-the-art accuracy but also a much better behaved surface representation whose differentiable properties can be estimated easily.

Our contribution is therefore a generic approach to leveraging 3D point cloud generating schemes so that the differential properties of the target surfaces are immediately available without further post-processing, which makes them usable by subsequent algorithms that perform tasks such as shape-from-shading, texture mapping, surface normal estimation from range scans [2, 19], and detail-preserving re-meshing [8].

The code is publicly available on our project page[1].

2. Related Work

Deep generative approaches for surface reconstruction. Modern generative Deep Nets are very good at reconstructing 3D surfaces for tasks such as shape completion from incomplete data [11, 26, 30, 28], single-view shape reconstruction [16, 25, 6, 14], and auto-encoding point-clouds [16, 13]. They represent the surfaces in terms of voxels [32, 30, 15], triangular meshes [25, 6, 12], or point clouds [16, 13, 14]. The common denominator of all these methods is that they deliver precise shapes in terms of 3D locations but not necessarily in terms of differential surface properties, such as normals and curvature. The latter may be inaccurate and even nonsensical as will be shown in the experiment section.

Patch-based representations. Among all these methods, FoldingNet [33] was the first to introduce the idea of learning a parametric mapping from a 2D patch to a 3D surface. It relies on a discrete sampling and follow-up methods introduced continuous multi-patch representations that are trained by minimizing the Chamfer distance [16, 13], a shape aware variant of the L2 distance [29], or are optimized to predict a single sample using Earth mover's distance[31]. One of the biggest advantage of these approaches is that the learned mapping, being a continuous function, allows for arbitrary sampling resolution at test time. However, still none of these methods gives access to the differential surface properties. An exception is the approach of [21] that learns a parameterization for B-spline approximation but only works with 2D curves.

Using differential surface properties for training. There are a few deep learning techniques that use differential surface properties in the form of either normal maps [6, 3] or their approximations computed on triangular meshes [17] but none that rely on 3D point clouds. Using differential surface properties still mostly belongs to the realm of non-deep learning methods, for example for shape from template [22, 5] or non-rigid structure-from-motion [1, 24], which are beyond the scope of this paper.

3. Multi Patch Representations

As discussed above, multi-patch representations [16, 31] are powerful tools for generating surfaces from latent representations. However, they suffer from a number of limitations that we discuss below and will address in Section 4.

3.1. Formalization

Let us consider a mapping $\mathcal{F}$ from a given low-dimensional latent vector $\mathbf{d} \in \mathbb{R}^D$ to a surface $\mathcal{S}$ in 3D space represented by a cloud of 3D points. In the multi-patch approach, the point cloud is taken to be the union of points generated by K independent mappings $f_{\mathbf{w}_k} : \mathbb{R}^D \times \mathcal{D}_f \rightarrow \mathbb{R}^3$ for $1 \leq j \leq K$, where each $f_{\mathbf{w}_k}$ is a trainable network with parameters $\mathbf{w}_k$ and $\mathcal{D}_f = [c_{\text{min}}, c_{\text{max}}]^2$ represents a square in $\mathbb{R}^2$. In other words, the $f_{\mathbf{w}_k}$ network takes as input a latent vector $\mathbf{d}$ and a 2D point in $\mathcal{D}_f$ and returns a 3D point.

Given a training set containing many 3D shapes, the network weights $\mathbf{w}_k$ are learned by minimizing a sum of Chamfer distance losses, one for each 3D shape in a training batch, of the form

$$\begin{aligned}\mathcal{L}_{\text{CHD}} = & \frac{1}{KM} \sum_{k=1}^{K} \sum_{i=1}^{M} \min_{j} \left\| \mathbf{p}_i^{(k)} - \mathbf{q}_j \right\|^2 + \\ & \frac{1}{N} \sum_{j=1}^{N} \min_{i,k} \left\| \mathbf{p}_i^{(k)} - \mathbf{q}_j \right\|^2 ,\end{aligned} \tag{1}$$

where M is the number of points predicted by each patch, N is the number of GT points, $\mathbf{p}_i^k$ is the i-th 3D point predicted by $f_{\mathbf{w}_k}$, and $\mathbf{q}_j$ is the j-th GT point. The whole pipeline is depicted in Figure 4.

3.2. Limitations

Minimizing the loss function of Eq. 1 yields patches that jointly cover the whole surface but does not constrain how

[1] https://github.com/bednarikjan/differential_surface_representation

much deformation individual patches undergo or how they are positioned with respect to each other. In practice, this leads to two potential failure modes.

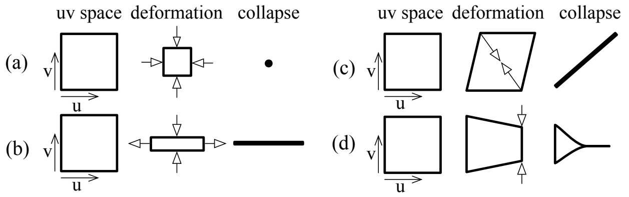

Figure 2. **2D representation of typical patch collapses.** (a) 0D collapse, (b) 1D stretch collapse, (c) 1D skew collapse and (d) partial collapse.

Patch Collapse. Some of the patches might collapse to undesirable configurations, such as those shown in Figure 2. This may not increase the total $\mathcal{L}_{\text{CHD}}$ value much when training is complete because the remaining, non-collapsed patches can compensate for the collapsed ones. However, collapsed patches still cause two main problems. First, their normals and curvature do not make sense anymore. Second, the $f_{\mathbf{w}_j}$ corresponding to a collapsed patch becomes useless, thus wasting the representational power of $\mathcal{F}$.

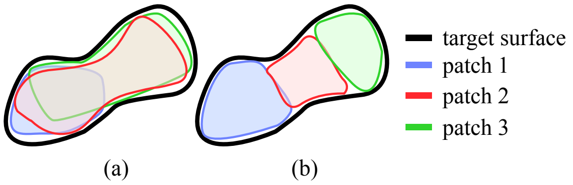

Figure 3. **Patch overlap**. (a) Up to 3-fold overlap. (b) Configuration with small overlap.

Patch Overlap. Another drawback of this approach is that it provides no control over the relative spatial configuration of the patches. Thus, it does not prevent them from overlapping each other, as depicted by Figure 3. This is an undesirable behavior because the overlapping patches may yield surfaces that are not well aligned and, again, because some of the expressive power of $\mathcal{F}$ is wasted.

4. Accounting for Differential Properties

We have seen that multi-patch representations are powerful but are subject to patch collapse and overlap, both of which reduce their expressive power. We now show that by regularizing the differential properties of the reconstructed surfaces during training, we can eliminate patch collapse and mitigate patch overlap. We will demonstrate in Section 5 that this boosts the accuracy of normals and curvature.

In the remainder of this section, we first explain how we can compute online the differential properties of surfaces represented by a 3D point cloud. We then present our approach to using them during training.

4.1. Differential Surface Properties

Let $\mathbf{r} = [u, v] \in \mathcal{D}_f$, where $\mathcal{D}_f$ is the 2D domain over which $f_{\mathbf{w}_k}$ is defined, as explained at the beginning of Section 3.1. $\mathbf{p} = f_{\mathbf{w}_k}(\mathbf{r})$ is a point of surface $\mathcal{S}$. We can compute the differential properties of $\mathcal{S}$, including normals and curvatures, from the derivatives of $f_{\mathbf{w}_k}$ with respect to u and v as follows, given that $f_{\mathbf{w}_k}$ is a continuously differentiable function. For notational simplicity, we drop the subscript $\mathbf{w}_k$ from $f_{\mathbf{w}_k}$ in the remainder of this section.

Let $\mathbf{J} = \begin{bmatrix}\mathbf{f}_u & \mathbf{f}_v\end{bmatrix}$ be the Jacobian of f at $\mathbf{p}$, where $\mathbf{f}_u = \frac{\partial f}{\partial u}$ and $\mathbf{f}_v = \frac{\partial f}{\partial v}$. The normal vector is

$$\mathbf{n} = \frac{\mathbf{f}_u \times \mathbf{f}_v}{\|\mathbf{f}_u \times \mathbf{f}_v\|}. \tag{2}$$

The curvature, area and deformation properties can be computed from the *metric tensor*

$$g = \mathbf{J}^\top \mathbf{J} = \begin{bmatrix}\mathbf{f}_u^\top \mathbf{f}_u & \mathbf{f}_u^\top \mathbf{f}_v \\ \mathbf{f}_u^\top \mathbf{f}_v & \mathbf{f}_v^\top \mathbf{f}_v\end{bmatrix} = \begin{bmatrix}E & F \\ F & G\end{bmatrix}. \tag{3}$$

The mean and Gaussian curvature are then

$$c_{\text{mean}} = -\frac{1}{2\det g}\mathbf{n}^\top \left[\frac{\partial^2 f}{\partial u^2}G - 2\frac{\partial^2 f}{\partial u \partial v}F + \frac{\partial^2 f}{\partial v^2}E\right], \tag{4}$$

$$c_{\text{gauss}} = \frac{\frac{\partial^2 f}{\partial u^2}^\top \mathbf{n} \cdot \frac{\partial^2 f}{\partial v^2}^\top \mathbf{n} - (\frac{\partial^2 f}{\partial u \partial v}^\top \mathbf{n})^2}{EG - F^2}. \tag{5}$$

Furthermore, the area of the surface covered by the patch can be estimated as

$$A = \iint_{\mathcal{D}_f} \sqrt{EG - F^2} du dv. \tag{6}$$

Note that all these surface properties are computed *analytically*. Thus they are *exact*, differentiable, and do not require a triangulation. This is unlike traditional methods that *approximate* these quantities on a point cloud or a mesh.

4.2. Learning a Robust Mapping

Recall that our goal is to learn a mapping $\mathcal{F}$ from multiple 2D patches to a 3D point cloud. In particular, we seek to constrain the deformations modeled by $\mathcal{F}$ such that patch collapse is prevented but complex surfaces can still be represented accurately. We now discuss the deformation model that we rely on and then introduce the required training loss functions.

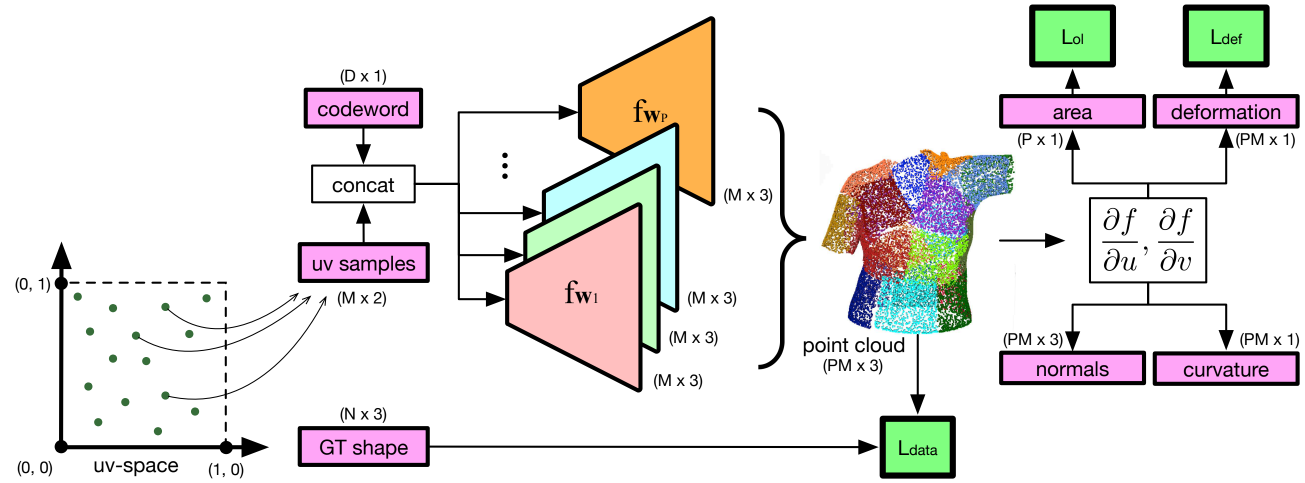

Figure 4. **Schematic view of our approach.** The input to the set of K decoders $\{f_{\mathbf{w}_k}\}$ is a latent vector $\mathbf{d}$ (dubbed *codeword*) and a set of 2D points sampled from the domain $\mathcal{D}_f$ (dubbed *uv-space*). The decoders produce point clouds, which together represent the target surface. The derivatives of $f_{\mathbf{w}_k}$ w.r.t. the *uv-space* allow for the analytical computation of each patch's area and deformation properties. The loss function used to train our model consists of a data term $\mathcal{L}_{\text{data}}$ using GT annotations and of terms $\mathcal{L}_{\text{ol}}$ and $\mathcal{L}_{\text{def}}$ which prevent patch overlap and patch collapse, respectively.

4.2.1 Deformation Model

Conformal mappings yield low distortions while retaining the capacity to model complex shapes. They are therefore widely used in computer graphics and computer vision, for example for texture mapping [9] and surface reconstruction [24]. For a surface to undergo conformal deformation, the metric tensor must be of the form

$$g_{\text{conf}} = s(\mathbf{r}) \begin{bmatrix} 1 & 0 \\ 0 & 1 \end{bmatrix}, \tag{7}$$

where $s : \mathcal{D}_f \rightarrow \mathbb{R}$ returns a scale value for each position in the parameter space. Unfortunately, making the deformation conformal does not prevent patch collapse, even in a single-patch scenario, since partial collapse can still occur wherever $s(\mathbf{r}_i) \sim 0$.

To address this, we propose to use *scaled isometric* mappings whose metric tensors can be written as

$$g_{\text{sciso}} = s \begin{bmatrix} 1 & 0 \\ 0 & 1 \end{bmatrix}, \tag{8}$$

where s is an unknown global scale shared by all parameter space locations. Constraining $\mathcal{F}$ to be a *scaled isometric* mapping amounts to assuming that the target surface is patch-wise developable, which has proved to be a reasonable assumption in the domain of deformable surface reconstruction [5, 4, 23].

In a single patch scenario, $s \sim 0$ is not an option anymore when minimizing the loss of Eq. 1 because the resulting surface would be point-collapsed and thus could not cover the full target surface. However, collapses can still occur in the multi-patch case, and have to be prevented using appropriate loss terms, as discussed below.

4.2.2 Loss Functions

Here, we formulate the loss terms that should be added to the data loss $\mathcal{L}_{\text{CHD}}$ of Eq. 1 during training to ensure that the resulting $f_{\mathbf{w}_k}$ represent scaled isometry, as described above, without patch collapse, and with as little overlap as possible.

Enforcing Conformality. We define

$$\mathcal{L}_E = \frac{1}{KM} \sum_{k=1}^{K} \sum_{i=1}^{M} \left(\frac{E_i^{(k)} - \mu_E}{A^{(k)}} \right)^2, \tag{9}$$

$$\mathcal{L}_G = \frac{1}{KM} \sum_{k=1}^{K} \sum_{i=1}^{M} \left(\frac{G_i^{(k)} - \mu_G}{A^{(k)}} \right)^2, \tag{10}$$

$$\mathcal{L}_{\text{sk}} = \frac{1}{KM} \sum_{k=1}^{K} \sum_{i=1}^{M} \left(\frac{F_i^{(k)}}{A^{(k)}} \right)^2, \tag{11}$$

$$\mathcal{L}_{\text{str}} = \frac{1}{KM} \sum_{k=1}^{K} \sum_{i=1}^{M} \left(\frac{E_i^{(k)} - G_i^{(k)}}{A^{(k)}} \right)^2, \tag{12}$$

where M is the number of points sampled on each surface patch; E, F, and G are defined in Eq. 3; $\mu_E = \frac{1}{KM} \sum_k \sum_i E_i^{(k)}$ and $\mu_G = \sum_k \sum_i G_i^{(k)}$; and $A^{(k)}$ is the area of a surface patch computed using Eq. 6. Note that we normalize these terms by $A^{(k)}$ to make them independent of the current surface patch area, which changes over the course of training.

Each one of these four losses controls the components of the metric tensor of Eq. 3, so that its off-diagonal terms are close to 0 and its diagonal terms are equal as in Eq 8. Concretely, $\mathcal{L}_{\text{str}}$ prevents a vertical or a horizontal stretch and thus, effectively, the 0D and 1D collapses shown in

Fig. 2(a,b). $\mathcal{L}_{\text{sk}}$ prevents 1D skew collapse as depicted by Fig. 2(c) while $\mathcal{L}_E$ and $\mathcal{L}_G$ prevent partial ones depicted by Fig. 2(d). Finally, we express our complete deformation loss as

$$\mathcal{L}_{\text{def}} = \alpha_E \mathcal{L}_E + \alpha_G \mathcal{L}_G + \alpha_{\text{sk}} \mathcal{L}_{\text{sk}} + \alpha_{\text{str}} \mathcal{L}_{\text{str}} \ , \qquad (13)$$

where $\alpha_E, \alpha_G, \alpha_{\text{sk}}, \alpha_{\text{str}} \in \mathbb{R}$ are hyperparameters.

Minimizing Overlaps. Recall from Section 4.1, that we can compute the area $A^{(k)}$ covered by a patch k using Eq. 6. We therefore introduce

$$\mathcal{L}_{\text{ol}} = \max\left(0, \sum_{k=1}^{K} \left(A^{(k)}\right) - \hat{A}\right)^2 \qquad (14)$$

to encourage the patches to jointly cover at most the area of the entire surface, where $\hat{A}$ is computed as the area of the GT mesh or of a triangulated GT depth map, depending on the task of interest. We estimate the patch area as $A^{(k)} = \frac{1}{M^{(k)}} \sum_{i=1}^{M^{(k)}} A_i^{(k)}$, where $M^{(k)}$ is the number of points sampled from the patch k and $A_i^{(k)}$ is Eq. 6 computed for a single point.

Combined Loss Function. We take our complete loss function to be

$$\mathcal{L} = \mathcal{L}_{\text{CHD}} + \alpha_{\text{def}} \mathcal{L}_{\text{def}} + \alpha_{\text{ol}} \mathcal{L}_{\text{ol}} \ , \qquad (15)$$

with hyperparameters $\alpha_{\text{def}}, \alpha_{\text{ol}} \in \mathbb{R}$. In practice, we use the weights of Eq. 13 to control the relative influence of the four terms of $\mathcal{L}_{\text{def}}$, and α_{def} and α_{ol} to control the overall magnitude of the deformation and overlap regularization term respectively.

4.2.3 Mapping Architecture

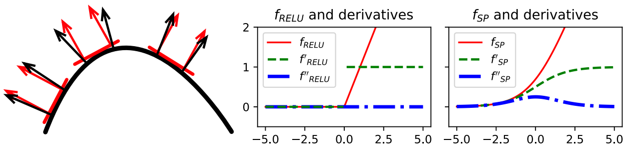

(a) (b) (c)

Figure 5. The use of the ReLU results in a piecewise linear mapping, which, as shown in red in (a), only poorly approximates the true surface normals (in black). As can be seen by comparing (b) and (c), the Softplus function approximates the ReLU behavior, while having smooth 1st and 2nd order derivatives.

As in [16], we implement each mapping $f_{\mathbf{w}_k}$ as a multilayer perceptron (MLP), with each MLP having its own set of weights. As we need $f_{\mathbf{w}_k}$ to be at least C^2-differentiable, we cannot use the popular ReLU activation function, which is C^2 only *almost* everywhere. Note that the ReLU function would also yield a piecewise linear mapping, which would be ill-suited to compute surface curvatures. Therefore, we use the *Softplus* function, which approximates the ReLU while having smooth 1st and the 2nd order derivatives, as shown in Figure 5.

5. Experiments

Our approach is generic and can thus be applied to different tasks relying on different architectures. We discuss them below, and then introduce the datasets and metrics we use for testing purposes. Finally, we present our results.

5.1. Tasks

We experimented with three popular surface reconstruction tasks, which we describe below, together with the architectures we used to tackle them.

Point Cloud Autoencoding (PCAE). We rely on an AtlasNet [16] variant in which we slightly modified the decoder: The ReLU activations are replaced with Softplus for the reasons stated in Section 4.2.3 and the last activation is linear. We removed the batch normalization layers because they made our training unstable.

Shape completion (SC). Given a partial 3D point cloud, such as a depth map, shape completion aims to predict a complete object shape. To this end, we use a U-Net [27] encoder that produces a latent representation $\mathbf{d}$ of size 2048 and the FoldingNet [33] decoder with all the activations replaced with Softplus except the last one which is linear.

Single-View 3D Shape Reconstruction (SVR). The goal of this task is to predict the shape of a surface observed in a single RGB image. To this end, we use an encoder implemented as a ResNet [18] with bottleneck modules and 44 layers and a decoder implemented as a FoldingNet [33] variant similar to the one used for **SC**. For the sake of fair comparison with the SotA, we also experimented with a variant of AtlasNet [16] with the same modifications as in **PCAE**.

In the remainder of this section, regardless of the task at hand, we will refer to our model which we train using $\mathcal{L}$ of Eq. 15 as **OURS**. For every experiment we report what values we used for the hyperparameters α_{def} and α_{ol} of Eq. 15. Unless stated otherwise, we set all the hyperparameters of Eq 13 to be equal to 1.

5.2. Datasets

ShapeNet Core v2 [10] (SN). This dataset consists of synthetic objects of multiple categories and has been widely used to gauge the performance of 3D shape reconstruction approaches. We use the same train/test split as in the AtlasNet paper [16].

Textureless deformable surfaces [6] (TDS). This real-world dataset of deformable surfaces captured in various lighting conditions consists of sequences of RGB images and corresponding depth and normal maps of 5 different objects. We selected the 2 for which the most data samples are available, a piece of cloth and a T-Shirt imaged with a single light setup. We use 85% of the samples for training, 5% for validation, and 10% for testing. The splits were created so that the validation and testing samples are as different as possible from the training ones. More details are provided in the supplementary material.

Female T-Shirts [17] (FTS). This synthetic dataset comprises T-Shirts worn by 600 different women in different poses. We randomly split the body shapes into training (87%), validation (8%) and testing (5%) sets. We precomputed the mean and Gaussian curvature on the GT meshes using quadric fitting implemented in the graphics library libigl [20].

5.3. Metrics

We report our results in terms of the following metrics.

Chamfer Distance (CHD). This distance is given in Eq. 1.

Mean ($\mathbf{m_H}$) and Gaussian ($\mathbf{m_K}$) Curvature. The curvatures are given in Eq. 4 and 5.

Angular error ($\mathbf{m_{ae}}$). To measure the accuracy of the computed normals, we define the mean angular error as $m_{ae} = \frac{1}{M}\sum_{i=1}^{M} \arccos|\mathbf{n}_i\hat{\mathbf{n}}_i|$, where $\mathbf{n}_i$ and $\hat{\mathbf{n}}_i$ are the unit length normals of a predicted point and its closest GT point. The absolute value is taken to make the metric invariant to the patch orientation, which neither our method nor the SotA approaches controls.

Number of collapsed patches ($\mathbf{m_{col}}$) We assume a patch k to be collapsed if $A^{(k)} < c_A\mu_A$, where $\mu_A = \sum_{k=1}^{K} A^{(k)}$ is the mean patch area and c_A is a constant to be chosen. We define the patch collapse metric as $m_{\text{col}} = \frac{1}{S}\sum_{s=1}^{S}\sum_{k=1}^{K}\mathbb{I}_{\left[A_s^{(k)}<c_A\mu_A\right]}$, that is, an average number of collapsed patches over a dataset of size S. In all our experiments, we set $c_A = 0.001$.

Amount of overlap ($\mathbf{m_{olap}^{(t)}}$). For each ground-truth 3D point, we count the number of patches within a predefined distance t and take the average over all the points.

5.4. Normal and Curvature Estimates

As discussed in 3.2, collapsed patches can strongly affect the quality of the normals and curvatures we can recover from estimated surfaces. **OURS** for **SC** on FTS prevents the collapses from happening. To demonstrate this, we trained the network also without the deformation loss $\mathcal{L}_{\text{def}}$ term of Eq. 13, to which we refer as **BASIC**. We used the FTS dataset for all our experiments. For training we randomly sampled 8000 GT points and the same number is predicted by **OURS** and **BASIC**.

We set $\alpha_{\text{def}} = 0.001$ and $\alpha_{\text{ol}} = 0$, thus ignoring overlaps, in Eq. 15 and the number of patches to 25. We report the results in Table 1 and Fig. 6 depicts typical collapse cases. Because there are no collapses for **OURS**, the resulting accuracy is improved, which validates our hypothesis that allowing patches to collapse wastes some of the networks descriptive power. Furthermore, the quality improvement of the computed normals is all the more significant. By contrast, *not* using the $\mathcal{L}_{\text{def}}$ makes the normals and curvatures, computed using Eq. 2, 4 and 5, useless, as illustrated by Fig. 6.

Table 1. **Training with (OURS) and without $\mathcal{L}_{\text{def}}$ (BASIC)** for **SC** on the FTS dataset. The CHD is multiplied by 10^3 and the m_{ae} is expressed in degrees. Note that computing the curvatures on the surface obtained with the model trained without $\mathcal{L}_{\text{def}}$ suffers from numerical instabilities, which prevented us from reporting m_H value when not using $\mathcal{L}_{\text{def}}$.

Model	**CHD**	$\mathbf{m_{ae}}$	$\mathbf{m_H}$	$\mathbf{m_K}$	$\mathbf{m_{col}}$
BASIC	0.14	24.38	n/a	170e6	9
OURS	**0.11**	**5.94**	**35.29**	**53e3**	**0**

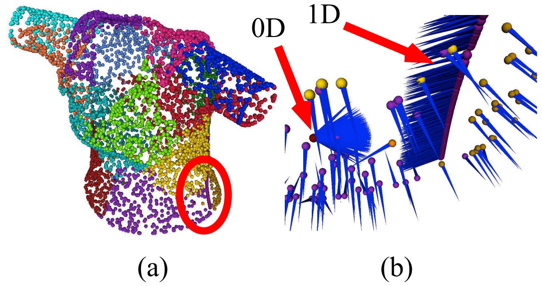

Figure 6. **Typical cases of 0D and 1D collapses.** (a) Predicted point cloud with different colors denoting the individual patches. The red ellipse focuses on a collapsed region. (b) Close up view of the 0D and 1D collapses and corresponding normals.

5.5. Number of Patches and Collapse

It could be argued that the patch collapse problems described above when not enforcing the regularization constraints are simply a consequence of using too many patches and that using fewer would cure the problem. We now show this not to be the case.

We trained **OURS** for **SVR** and, as before, we also trained **BASIC**, that is, no $\mathcal{L}_{\text{def}}$ term. We used the TDS dataset for all our experiments. For training, we sampled 3000 points randomly from the GT depth map and the same number is predicted by our model. As before, we set $\alpha_{\text{def}} = 0.001$ and $\alpha_{\text{ol}} = 0$. In Table 2 we show that regardless of the number of patches, the collapses always occur when using **BASIC** and never when using **OURS**. While CHD is comparable for both models, the angular error is always lower for **OURS**.

Table 2. **Training the model with (OURS) and without $\mathcal{L}_{\text{def}}$ (BASIC)** for **SVR** on the TDS dataset. Note that the normals are much more accurate when using $\mathcal{L}_{\text{def}}$.

	Cloth				T-Shirt			
Model	**# patch.**	**CHD**	$\mathbf{m_{ae}}$	$\mathbf{m_{col}}$	**# patch.**	**CHD**	$\mathbf{m_{ae}}$	$\mathbf{m_{col}}$
BASIC	2	0.36	30.32	1	2	**0.48**	48.32	1
OURS	2	**0.33**	**20.90**	**0**	2	0.51	**20.35**	**0**
BASIC	3	0.35	21.95	1	3	0.46	36.29	1
OURS	3	**0.32**	**20.60**	**0**	3	**0.49**	**20.44**	**0**
BASIC	4	**0.37**	28.77	2	4	**0.41**	22.95	1
OURS	4	0.39	**21.08**	**0**	4	0.42	**20.77**	**0**
BASIC	10	**0.33**	25.67	2.02	15	**0.41**	23.51	2
OURS	10	0.41	**20.17**	**0**	15	**0.41**	**20.93**	**0**

5.6. Comparison to the SotA on PCAE and SVR

Here we compare the predictions delivered by **OURS** against those delivered by AtlasNet [16] (AN) on two tasks, **PCAE** on the ShapeNet dataset and **SVR** on the TDS dataset. In both cases, our goal is not only to minimize CHD but also to minimize patch overlap. We again set $\alpha_{\text{def}} = 0.001$ but now turn on the $\mathcal{L}_{\text{ol}}$ loss by setting $\alpha_{\text{ol}} = 0.1$.

PCAE on ShapeNet. We retrained the original AN using the code provided by the authors and trained **OURS** on **PCAE** using the ShapeNet dataset separately on object categories airplane, chair, car, couch and cellphone and jointly on all these categories. We used 25 patches, 2500 points randomly sampled from the GT point clouds and the same amount is predicted by **OURS** and AN. Since the ShapeNet objects often contain long thin parts (e.g. legs of a chair or wings of an airplane) we chose to allow patch stretching and set α_{str} of Eq. 13 to 0. We trained both **OURS** and AN until convergence.

We report our results in Table 3. Note that **OURS** delivers comparable CHD precision while achieving significantly less overlap and higher normals accuracy as quantified by metrics m_{olap} and m_{ae}. Fig. 7 depicts the mean overlap as a function of the neighborhood size threshold t used to compute $m_{\text{olap}}^{(t)}$. Our approach consistently reduces the overlap, as illustrated by Fig. 8.

SVR on TDS. We ran two separate experiments on the T-Shirt and the Cloth. We use 4 patches for the former as the object represents a simple rectangular shape and 14 for the latter as the T-Shirt is more complex.We trained AN using the code provided by the authors. For both **OURS** and AN, we used 8000 points randomly sampled from the GT and the same number is predicted by the networks. We trained both **OURS** and AN until convergence.

Table 3. **OURS vs AN trained for PCAE.** Both models were trained individually on 5 ShapeNet categories (plane, chair, car, couch, cellphone) and jointly on all of them (all). While CHD is comparable for both methods, **OURS** delivers better normals and lower patch overlap.

obj.	**method**	**CHD**	$\mathbf{m_{ae}}$	$m_{\text{olap}}^{(0.01)}$	$m_{\text{olap}}^{(0.05)}$	$m_{\text{olap}}^{(0.1)}$	$\mathbf{m_{col}}$
plane	AN	**1.07**	21.26	5.90	12.08	15.39	0.006
	OURS	1.08	**17.90**	**3.82**	**7.99**	**10.88**	**0.000**
chair	AN	**2.79**	24.49	5.30	9.45	12.12	0.011
	OURS	2.82	**23.06**	**2.85**	**5.78**	**8.09**	**0.000**
car	AN	4.68	18.08	4.61	9.07	12.50	0.011
	OURS	**3.34**	**17.75**	**2.50**	**4.85**	**7.26**	**0.000**
couch	AN	**2.10**	16.83	3.74	8.07	11.67	**0.000**
	OURS	2.21	**14.90**	**2.54**	**5.41**	**8.08**	**0.000**
cellphone	AN	**1.80**	10.29	6.51	13.65	16.79	**0.000**
	OURS	1.82	**9.64**	**2.75**	**6.13**	**8.69**	**0.000**
all	AN	**2.51**	24.55	7.69	13.28	16.23	0.280
	OURS	2.91	**23.12**	**3.37**	**6.67**	**9.10**	**0.000**

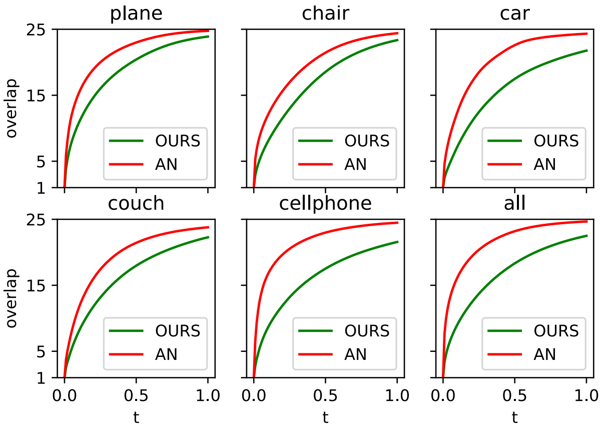

Figure 7. **Patch overlap for OURS and AN** trained for **PCAE** on the ShapeNet dataset. We plot $m_{\text{col}}^{(t)}$ as a function of t.

We report the results in Table 4. The results show the same trends as in the previous example, with a similar accuracy in terms of CHD but a higher normal accuracy and much less overlap for **OURS**. The qualitative results are depicted in Fig. 10 and the amount of overlap is quantified in Fig. 9. Note that in this case, AN suffers a number of patch collapses whereas **OURS** does not, which means that if the normals and curvature were needed for future processing our approach would be the better option. Besides the obvious 0D point collapses, the predictions of AN also suffer less visible but equally harmful partial collapses as demonstrated in Fig. 11.

Approximate normal estimation. When the normals cannot be computed analytically using Eq. 2, one can resort to an approximate method, such as the covariance-based approach [7] popular in vision and robotics. However, such an ad-hoc post-processing step is costly and sensitive to the value of a hyperparameter. For the sake of completeness, we computed approximate normals from the AN predictions in

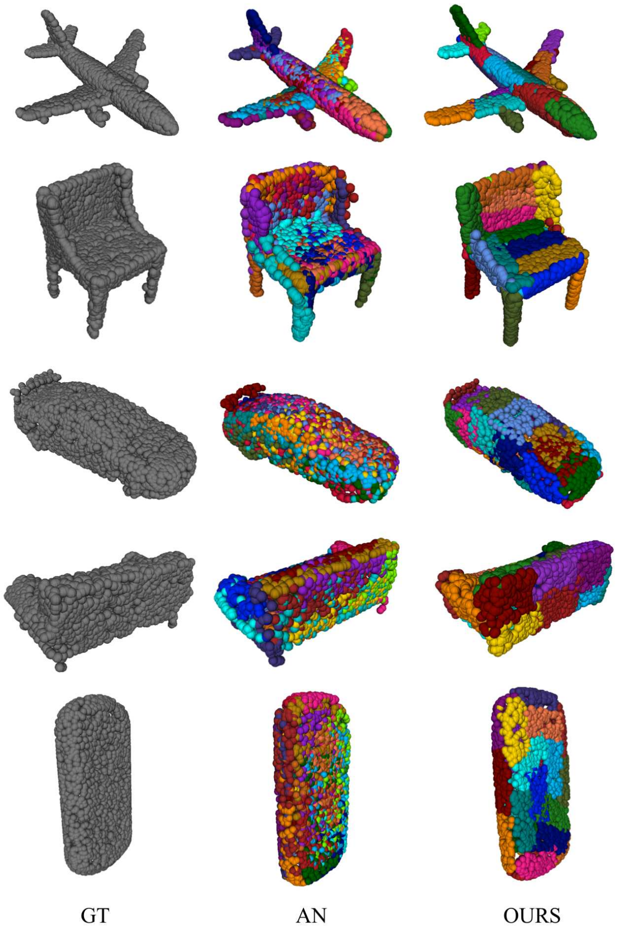

Figure 8. **OURS vs AN trained for PCAE** on individual ShapeNet categories. Each color denotes the points generated by one patch. Those generated by our approach are much better organized with far less overlap.

Table 4. **OURS vs AN on SVR for 2 objects from the TDS dataset.** As before CHD is comparable for both methods, but **OURS** delivers better normals and less patch overlap.

object	method	CHD	m_{ae}	$m_{\text{olap}}^{(0.001)}$	$m_{\text{olap}}^{(0.005)}$	$m_{\text{olap}}^{(0.05)}$	$\mathrm{m}_{\mathrm{col}}$
cloth	AN	**0.26**	47.42	3.06	3.19	3.76	2
	OURS	0.28	**20.06**	**1.37**	**1.75**	**3.53**	**0**
tshirt	AN	0.35	42.12	8.95	10.03	12.64	7
	OURS	**0.31**	**20.52**	**1.80**	**2.89**	**8.22**	**0**

both aforementioned experiments and show in the supplementary material that their accuracy is markedly inferior to our analytically computed ones in all but one experiment.

6. Conclusion

We have presented a novel and generic deep learning framework for 3D cloud point generation that makes it possible to compute analytically the differential properties of the surface the 3D points represent, without any need for post-processing. Our approach is inspired by the multi-patch approach of [16] and we have shown that we can use those differential properties during training to reduce the amount of patch overlap while delivering usable normals and curvatures, which the original approach does not do.

In future work, we will incorporate this framework in end-to-end trainable networks that require the differential properties to exploit the image information and to perform tasks such as shape-from-shading or texture mapping.

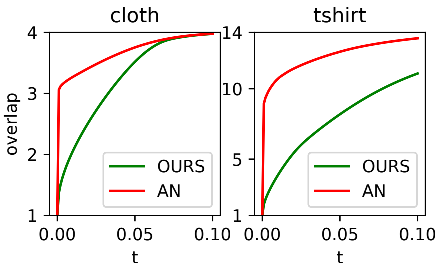

Figure 9. **Patch overlap for OURS and AN** trained for **SVR** on the TDS dataset. We plot $m_{\text{col}}^{(t)}$ as a function of t.

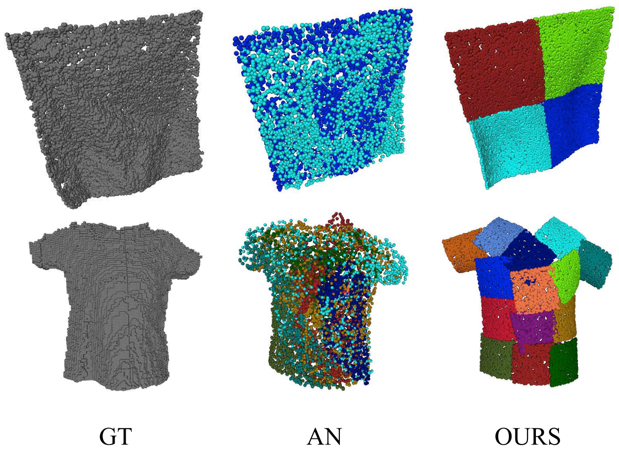

Figure 10. **OURS vs AN trained for SVR** on the TDS dataset. Each color denotes the points generated by one patch. Those generated by our approach are much better organized with far less overlap and no collapsed patches.

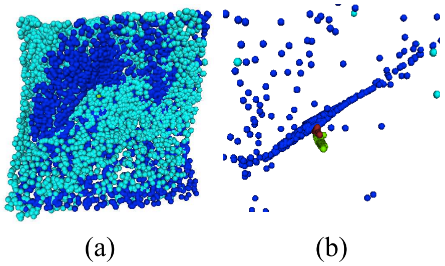

Figure 11. **Partial collapse.** Even though the dark blue patch predicted by AN seems to be well developed (a), a zoomed in view reveals a partial collapse (b).

References

[1] A. Agudo, F. Moreno-Noguer, B. Calvo, and J. M. M. Montiel. Sequential Non-Rigid Structure from Motion Using Physical Priors. *IEEE Transactions on Pattern Analysis and Machine Intelligence*, 38(5):979–994, 2016. 2

[2] H. Badino, D. Huber, Y. Park, and T. Kanade. Fast and Accurate Computation of Surface Normals from Range Images. In *2011 IEEE International Conference on Robotics and Automation*, 2011. 2

[3] A. Bansal, B. Russell, and A. Gupta. Marr Revisited: 2D-3D Model Alignment via Surface Normal Prediction. In *Conference on Computer Vision and Pattern Recognition*, 2016. 2

[4] A. Bartoli, Y. Gérard, F. Chadebecq, and T. Collins. On Template-Based Reconstruction from a Single View: Analytical Solutions and Proofs of Well-Posedness for Developable, Isometric and Conformal Surfaces. In *Conference on Computer Vision and Pattern Recognition*, 2012. 4

[5] A. Bartoli, Y. Gérard, F. Chadebecq, T. Collins, and D. Pizarro. Shape-From-Template. *IEEE Transactions on Pattern Analysis and Machine Intelligence*, 2015. 2, 4

[6] J. Bednarík, M. Salzmann, and P. Fua. Learning to Reconstruct Texture-Less Deformable Surfaces. In *International Conference on 3D Vision*, 2018. 2, 6

[7] J. Berkmann and T. Caelli. Computation of surface geometry and segmentation using covariance techniques. *PAMI*, 1994. 7

[8] D. Bommes, B. Lévy, N. Pietroni, E. Puppo, C. Silva, M. Tarini, and D. Zorin. Quad-Mesh Generation and Processing: A Survey. *Computer Graphics Forum*, 32(6):51–76, September 2013. 2

[9] Mario Botsch, Leif Kobbelt, Mark Pauly, Pierre Alliez, and Bruno Lévy. *Polygon Mesh Processing*. AK Peters / CRC Press, 2010. 4

[10] A. Chang, T. Funkhouser, L G., P. Hanrahan, Q. Huang, Z. Li, S. Savarese, M. Savva, S. Song, H. Su, J. Xiao, L. Yi, and F. Yu. Shapenet: An Information-Rich 3D Model Repository. In *arXiv Preprint*, 2015. 1, 5

[11] A. Dai, C. Qi, and M. Nießner. Shape Completion Using 3D-Encoder-Predictor CNNs and Shape Synthesis. In *Conference on Computer Vision and Pattern Recognition*, 2017. 2

[12] R. Danerek, E. Dibra, C. öztireli, R. Ziegler, and M. Gross. Deepgarment : 3D Garment Shape Estimation from a Single Image. *Eurographics*, 2017. 2

[13] T. Deprelle, T. Groueix, M. Fisher, V. G. Kim, B. C. Russell, and M. Aubry. Learning Elementary Structures for 3D Shape Generation and Matching. In *Advances in Neural Information Processing Systems*, 2019. 2

[14] H. Fan, H. Su, and L. Guibas. A Point Set Generation Network for 3D Object Reconstruction from a Single Image. In *Conference on Computer Vision and Pattern Recognition*, 2017. 2

[15] M. Firman, O.M. Aodha, S. Julier, and G.J. Brostow. Structured Completion of Unobserved Voxels from a Single Depth Image. In *Conference on Computer Vision and Pattern Recognition*, 2016. 2

[16] T. Groueix, M. Fisher, V. Kim, B. Russell, and M. Aubry. Atlasnet: A Papier-Mâché Approach to Learning 3D Surface Generation. In *Conference on Computer Vision and Pattern Recognition*, 2018. 1, 2, 5, 7, 8

[17] E. Gundogdu, V. Constantin, A. Seifoddini, M. Dang, M. Salzmann, and P. Fua. Garnet: A Two-Stream Network for Fast and Accurate 3D Cloth Draping. In *International Conference on Computer Vision*, 2019. 2, 6

[18] K. He, X. Zhang, S. Ren, and J. Sun. Deep Residual Learning for Image Recognition. In *Conference on Computer Vision and Pattern Recognition*, pages 770–778, 2016. 5

[19] S. Holzer, R. B. Rusu, M. Dixon, S. Gedikli, and N. Navab. Adaptive Neighborhood Selection for Real-Time Surface Normal Estimation from Organized Point Cloud Data Using Integral Images. In *International Conference on Intelligent Robots and Systems*, 2012. 2

[20] Alec Jacobson, Daniele Panozzo, et al. libigl: A simple C++ geometry processing library, 2018. https://libigl.github.io/. 6

[21] P. Laube, M. O. Franz, and G. Umlauf. Deep Learning Parametrization for B-Spline Curve Approximation. In *3DV*, 2018. 2

[22] D. Ngo, J. Ostlund, and P. Fua. Template-Based Monocular 3D Shape Recovery Using Laplacian Meshes. *IEEE Transactions on Pattern Analysis and Machine Intelligence*, 38(1):172–187, 2016. 2

[23] D. Ngo, S. Park, A. Jorstad, A. Crivellaro, C. Yoo, and P. Fua. Dense Image Registration and Deformable Surface Reconstruction in Presence of Occlusions and Minimal Texture. In *International Conference on Computer Vision*, 2015. 4

[24] S. Parashar, D. Pizarro, and A. Bartoli. Local Deformable 3D Reconstruction with Cartan's Connections. *IEEE Transactions on Pattern Analysis and Machine Intelligence*, 2019. 2, 4

[25] A. Pumarola, A. Agudo, L. Porzi, A. Sanfeliu, V. Lepetit, and F. Moreno-Noguer. Geometry-Aware Network for Non-Rigid Shape Prediction from a Single View. In *Conference on Computer Vision and Pattern Recognition*, June 2018. 2

[26] J. Rock, T. Gupta, J. Thorsen, J. Gwak, D. Shin, and D. Hoiem. Completing 3D Object Shape from One Depth Image. In *Conference on Computer Vision and Pattern Recognition*, pages 2484–2493, 2015. 2

[27] O. Ronneberger, P. Fischer, and T. Brox. U-Net: Convolutional Networks for Biomedical Image Segmentation. In *Conference on Medical Image Computing and Computer Assisted Intervention*, pages 234–241, 2015. 5

[28] D. Shin, C. Fowlkes, and D. Hoiem. Pixels, Voxels, and Views: A Study of Shape Representations for Single View 3D Object Shape Prediction. In *Conference on Computer Vision and Pattern Recognition*, 2018. 2

[29] A. Sinha, A. Unmesh, Q.-X. Huang, and K. Ramani. Surfnet: Generating 3D Shape Surfaces Using Deep Residual Networks. In *Conference on Computer Vision and Pattern Recognition*, 2017. 2

[30] A.A. Soltani, H. Huang, J. Wu, T. D. Kulkarni, and J.B. Tenenbaum. Synthesizing 3D Shapes via Modeling Multi-View Depth Maps and Silhouettes with Deep Generative Networks. In *Conference on Computer Vision and Pattern Recognition*, pages 2511–2519, 2017. 2

[31] F. Williams, T. Schneider, C. T. Silva, D. Zorin, J. Bruna, and D. Panozzo. Deep Geometric Prior for Surface Reconstruction. In *Conference on Computer Vision and Pattern Recognition*, 2019. 2

[32] J. Wu, Y. Wang, T. Xue, X. Sun, W.T. Freeman, and J.B. Tenenbaum. Marrnet: 3D Shape Reconstruction via 2.5D Sketches. In *Advances in Neural Information Processing Systems*, 2017. 2

[33] Y. Yang, C. Feng, Y. Shen, and D. Tian. Foldingnet: Point Cloud Auto-Encoder via Deep Grid Deformation. In *Conference on Computer Vision and Pattern Recognition*, June 2018. 1, 2, 5